Real space observation of two-dimensional Bloch wave interferences in a negative index photonic crystal cavity

Loïc Lalouat,[1] Benoit Cluzel,[1,*] Laurent Salomon,[1] Colette Dumas,[1] Christian Seassal,[2] Nicolas Louvion,[2] Ségolène Callard,[2] and Frédérique de Fornel[1]

[1]*Groupe d'Optique de Champ Proche, Institut Carnot de Bourgogne (ICB), Université de Bourgogne, UMR CNRS 5209, 9 Avenue A. Savary, BP 47870, F-21078 Dijon, France*

[2]*Université de Lyon, Institut des Nanotechnologies de Lyon (INL), UMR CNRS 5270, Ecole Centrale de Lyon, 36 Avenue Guy de Collongue, F-69134 Ecully, France*

(Received 12 June 2008; revised manuscript received 9 October 2008; published 5 December 2008)

We report here the direct observation of two-dimensional (2D) Bloch wave interferences in a negative index photonic crystal by using optical near-field microscopy techniques. The photonic crystal is formed by a defectless honeycomb lattice of air holes etched in III-V semiconductor slab. A scanning near-field optical microscope is used to visualize spatially, as well as spectrally, the light distribution inside the photonic crystal. The recorded near-field spectra and maps presented here unambiguously demonstrate the Bloch wave interferences within the photonic crystal. Then, the spectral and spatial evolution of these interferences allows us to recover experimentally the 2D band diagram of the photonic crystal demonstrating that this structure operates in a negative refraction regime and acts as a left-handed cavity.

DOI: 10.1103/PhysRevB.78.235304 PACS number(s): 42.70.Qs, 07.79.Fc, 78.20.Ci, 78.67.−n

I. INTRODUCTION

Since the pioneering work of Veselago[1] who described in the 1960s the behavior of electromagnetic waves in a hypothetic negative refractive index material, the feasibility of such a material has been extensively studied for the past few years. As a matter of fact, these materials present remarkable properties to reverse several well-known physical effect such as Doppler effect, Varilov-Cerenkov effect, or Casimir effect as proposed recently.[2] In addition, as proposed by Pendry,[3] these materials may also find several applications to improve the existing optical systems since they could permit to overcome the diffraction limit. However, achieving a material with a negative refractive index requires artificial materials or metamaterials patterned at the subwavelength scale.[4] According to the scaling law of electromagnetism, this implies that metamaterials at optical frequencies are nanomaterials. In this field, the ability of semiconductor two-dimensional photonic crystals (2DPCs) to produce a negative refractive index has been demonstrated theoretically[5–7] as well as experimentally.[8,9]

In this work, we analyze experimentally the electromagnetic field distribution in the optical near field of such a photonic crystal (PC) with a negative refractive index. By using a scanning near-field optical microscope (SNOM), we demonstrate the role of the Bloch wave interferences on the spatial and spectral light distributions inside the PC optical near field. This analysis is supported by the comparison with the theoretical band diagram of the PC which is recovered experimentally in light of this interpretation.

II. SAMPLE DESCRIPTION

The 2DPC consists in a defectless honeycomb lattice of air holes etched in an InP slab using electron-beam (e-beam) lithography and reactive ion etching. Four InAsP quantum wells (QWs) separated by InP barrier layers are embedded inside the 250-nm-thick InP slab which is wafer bonded onto a 1-μm-thick SiO_2 layer on top of a silicon host substrate. The fabricated structure exhibits a minimal distance between two holes of $a=425$ nm with a hole diameter of $d=300$ nm. This corresponds to a period lattice of $\Lambda=735$ nm. Figure 1(a) shows a scanning electronic microscope (SEM) picture of the whole 2DPC structure which consists of a hexagon (with respect to the symmetry axis of

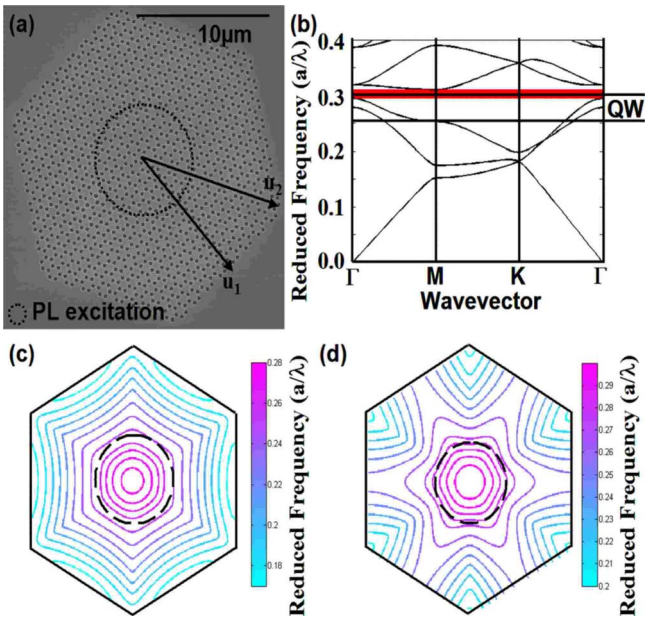

FIG. 1. (Color online) (a) Scanning electronic microscope image of the two-dimensional honeycomb photonic crystal structure. (b) TE band diagram of the honeycomb photonic crystal. The reduced frequency range corresponding to the quantum wells photoluminescence is indicated. [(c) and (d)] Equifrequency curves for the TE second and third bands. The black circle indicates the frequency domain studied in the near-field images presented in Figs. 4 and 5.

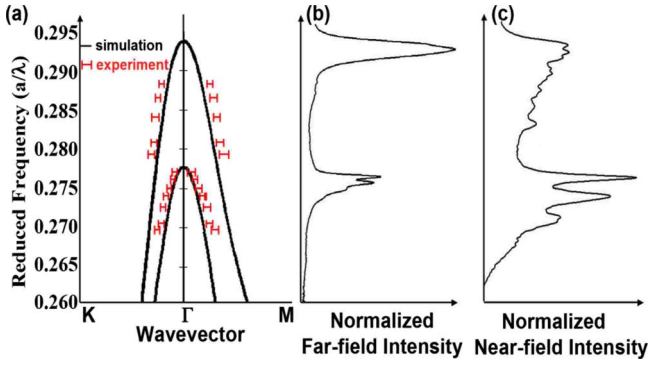

FIG. 2. (Color online) (a) Computed band diagram of the photonic crystal reduced to the second and third TE bands along the two directions of high symmetry of the honeycomb lattice. The experimental dispersion curves (markers) recovered in light of the near-field measurements are superimposed to the calculation. (b) Photoluminescence spectrum of the 2DPC recorded in far field with a numerical aperture of 0.22. (c) Photoluminescence spectrum of the 2DPC recorded in near field with a SNOM probe.

the honeycomb lattice) with a 24-period-long edge.

For such a honeycomb 2DPC, the TE band diagram [plotted in Fig. 1(b)] exhibits different domains where a negative refraction regime occurs.[10] In this work, we focused our attention on the second and third bands of the TE band diagram which operates in such a regime. The equifrequency curves corresponding to these two bands are plotted in Figs. 1(c) and 1(d). As illustrated in Fig. 1(b), the optogeometrical parameters of the fabricated structure were chosen in order to match the reduced frequency of these bands with the photoluminescence (PL) spectrum of the QWs ranging from 1250 to 1650 nm.

III. FAR-FIELD AND NEAR-FIELD SPECTROSCOPIES

We first characterized the structure using a usual PL setup operating in the optical far field. The 2DPC is illuminated with a focused red laser diode ($\lambda_{exc}=785$ nm) and the PL of the 2DPC, outcoupled into the far field, is collected with a numerical aperture of 0.22. The typical far-field spectrum is plotted in Fig. 2(b). As expected for such a PC structure, two intense PL peaks are recorded as the second and third bands crossing the Γ point of the Brillouin zone with a low group velocity.[11] These peaks are associated to the redistribution of the emission diagram of the 2DPC around the normal direction.[12] This confirms that the fabricated sample matches the condition between the QWs PL and the band positions. We next resort to the SNOM technique in order to directly probe the Bloch waves with a negative refractive index propagating inside the 2DPC. As a matter of fact, for the past few years, several studies have demonstrated the ability of this technique to directly examine the interactions between light and PC structures,[13–17] breaking over the far-field limitations.

A SNOM probe consisting of a chemically etched monomode silica fiber with a 100-nm-width apex is approached at a few nanometer height from the 2DPC and scanned over the surface using piezoelectric stages. A red laser diode is focused in a 8-μm-large spot in the middle of the structure, and the optical near-field spectra of the 2DPC are recorded for several positions of the probe.

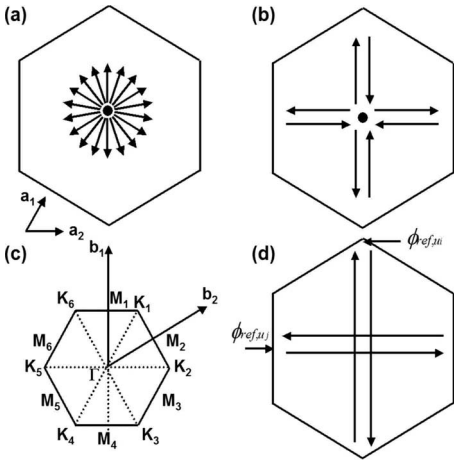

FIG. 3. (a) Emission of an initial Bloch wave in the middle of the structure along all the in-plane direction and with the same phase origin. (b) Privileged directions for interferences according to the structure geometry. (c) ΓM and ΓK directions of the photonic crystal lattice in the reciprocal space. The wave vector $\mathbf{G}_{m,n}$ is defined as $\mathbf{G}_{m,n}=m\times\mathbf{b_1}+n\times\mathbf{b_2}$, with $(\mathbf{b_1},\mathbf{b_2})$ as the vector of the reciprocal space associated to $(\mathbf{a_1},\mathbf{a_2})$, which is the vector of the direct space. (d) Phase origin for a given direction $\mathbf{u_i}$ imposed at one edge of the structure.

To allow for a direct comparison with the far-field spectrum, we plotted on Fig. 2(c) the typical near-field spectrum recorded with the probe positioned at the center of the structure. One can observe on the near-field measurement that the spectrum does not exhibit the sharp PL peaks observed in the far field but rather shows a continuum of PL peaks. These ones can no longer be associated to the flat and low group velocity band in the center of the Brillouin zone. As a matter of fact, in contrast to the far-field measurements, the near-field measurements are not limited by any numerical aperture and are sensitive to the electromagnetic waves propagating inside the 2DPC structure. As shown hereafter, the near-field PL peaks of Fig. 2(c) do not result anymore from any emission diagram redistribution as observed in far field but are associated to the Bloch wave properties inside the 2DPC.

IV. MODELIZATION OF THE CAVITY

Since the 2DPC has a finite size, the whole structure forms a hexagonal cavity which supports several standing two-dimensional Bloch waves resulting from the interferences between propagative and counterpropagative 2D Bloch waves. As depicted in Fig. 3(a), the initial propagative Bloch mode $E^i(\mathbf{r},\lambda)$ is excited in the middle of the structure and then propagates along all the in-plane direction. This can be expressed as

$$E_i(\mathbf{r},\lambda)=\int_{\theta=0}^{2\pi}\sum_m\sum_n E^0_{m,n}\exp[i(\mathbf{k}_\theta+\mathbf{G}_{m,n})\cdot\mathbf{r}]d\theta, \quad (1)$$

where $E^0_{m,n}$ is the amplitude of the (m^{st}, n^{st})-Bloch harmonic, $\mathbf{G}_{m,n}$ is the associated vector in the reciprocal space,

and the integration over θ represents the different in-plane propagation directions. According to the Snell-Descartes first law, each Bloch harmonic incoming on the edge of the whole structure is reflected in a well-defined direction. Thus, the total electrical field $E_t(\mathbf{r},\lambda)$ within the cavity is

$$E_t(\mathbf{r},\lambda) = \int_{\theta=0}^{2\pi} \sum_m \sum_n \{E^0_{m,n} \exp[i(\mathbf{k}_\theta + \mathbf{G}_{m,n}) \cdot \mathbf{r}] + E^1_{m,n} \exp[i(\mathbf{k}_\theta + \mathbf{G}_{m,n})_{\text{ref}} \cdot \mathbf{r} + i\varphi_{m,n,\theta}]\} d\theta, \quad (2)$$

where $E^1_{m,n}$ is the amplitude of the reflected $(m^{\text{st}},n^{\text{st}})$-Bloch harmonic, $(\mathbf{k}_\theta+\mathbf{G}_{m,n})_{\text{ref}}$ is the wave vector, and $\phi_{m,n,\theta}$ is the phase shift at reflection. Since the SNOM probe is selectively sensitive to the electrical field[16] of the Bloch waves, the light intensity locally detected by the SNOM probe, $I_s(\mathrm{r},\lambda)$, is

$$I_s(\mathrm{r},\lambda) = E_s(\mathbf{r},\lambda) \,.\, [E_s(\mathbf{r},\lambda)]^*, \quad (3)$$

with $E_s(\mathbf{r},\lambda)$ as the electrical field coupled into the SNOM probe which slightly differs from $E_t(\mathbf{r},\lambda)$ since it incorporates the coupling coefficiencies of the $(m^{\text{st}},n^{\text{st}})$-Bloch harmonic into the SNOM probe $\alpha_{(\mathbf{k}_\theta+\mathbf{G}_{m,n})}$.

In addition, since the cavity dimensions are much larger than the wavelength [almost 40 (λ_0/n)] and since the isofrequency contours are quasicircular in our range of investigation, the 2DPC can be considered as an isotropic homogeneous medium. Consequently, in regards to the geometry of the cavity the interferences between propagative and counterpropagative Bloch harmonics will present the maximum visibility along the high-symmetry direction of the structure, which corresponds to direct Fabry-Perot oscillations between two opposite edges and corners[18] [see Fig. 3(b)]. These directions correspond to the ΓM and ΓK high-symmetry directions of the PC lattice in the reciprocal space [Fig. 3(c)]. Since the PC exhibits a $C6$ symmetry, six different directions have to be considered independently [Fig. 3(c)]:

(i) The $\mathbf{u}_1=M_1-M_4$ direction which corresponds to a $(m^{\text{st}},n^{\text{st}})$-Bloch harmonic with $(m,n)=(m,0)$;

(ii) The $\mathbf{u}_2=M_2-M_5$ direction which corresponds to a $(m^{\text{st}},n^{\text{st}})$-Bloch harmonic with $(m,n)=(0,n)$;

(iii) The $\mathbf{u}_3=M_3-M_6$ direction which corresponds to a $(m^{\text{st}},n^{\text{st}})$-Bloch harmonic with $(m,n)=(m,-m)$;

(iv) The $\mathbf{u}_4=K_1-K_4$ direction which corresponds to a $(m^{\text{st}},n^{\text{st}})$-Bloch harmonic with $(m,n)=(m,m)$;

(v) The $\mathbf{u}_5=K_2-K_5$ direction which corresponds to a $(m^{\text{st}},n^{\text{st}})$-Bloch harmonic with $(m,n)=(m,-2m)$;

(vi) The $\mathbf{u}_6=K_3-K_6$ direction which corresponds to a $(m^{\text{st}},n^{\text{st}})$-Bloch harmonic with $(m,n)=(2m,-m)$.

Next, along the direction $\mathbf{u_i}$ of the PC, the phase origin is chosen at the edge of the structure [see in Fig. 3(d)] in order to define the phase shift $\phi_{m,n,\mathbf{u_i}}$ between the initial and reflected $(m^{\text{st}},n^{\text{st}})$-Bloch harmonics as $\phi_{m,n,\mathbf{u_i}}(\lambda) = (4\pi/\lambda) n^{\text{eff}}_{m,n,\mathbf{u_i}} L_{\mathbf{u_i}}$, with $L_{\mathbf{u_i}}$ as the length of the cavity and $n^{\text{eff}}_{m,n,\mathbf{u_i}}$ as the effective index of the $(m^{\text{st}},n^{\text{st}})$-Bloch harmonic along the direction $\mathbf{u_i}$. Consequently, the terms of Eq. (2) that lead to the interferences with the highest visibility are limited to $E_{\text{int},\mathbf{u_i}}(\mathbf{r},\lambda)$;

$$E_{\text{int},\mathbf{u_i}}(\mathbf{r},\lambda) = \sum_{m,n,\text{condition for } \mathbf{u_i}} E^0_{m,n} \exp[i(\mathbf{k}_{\mathbf{u_i}} + \mathbf{G}_{m,n}) \cdot \mathbf{r}] + \sum_{m,n,\text{condition for } \mathbf{u_i}} E^1_{m,n} \exp[-i(\mathbf{k}_{\mathbf{u_i}} + \mathbf{G}_{m,n}) \cdot \mathbf{r} + i\varphi_{m,n,\theta}]. \quad (4)$$

Thus, taking into account the coupling efficiency of the Bloch harmonics inside the near-field probe, the intensity, $I_{\text{int},\mathbf{u_i}}(\mathbf{r},\lambda)$, of the corresponding detected light is

$$\begin{aligned} I_{\text{int},\mathbf{u_i}}(\mathbf{r},\lambda) = & \sum_{m1,n1,cd\mathbf{u_i}} \sum_{m2,n2,cd\mathbf{u_i}} \alpha_{\mathbf{k}_{\mathbf{u_i}}+\mathbf{G}_{m1,n1}} \alpha_{\mathbf{k}_{\mathbf{u_i}}+\mathbf{G}_{m2,n2}} E^0_{m1,n1} E^0_{m2,n2} \exp(i\mathbf{G}_{m1-m2,n1-n2} \cdot \mathbf{r}) \\ & + \sum_{m1,n1,cd\mathbf{u_i}} \sum_{m2,n2,cd\mathbf{u_i}} \alpha_{\mathbf{k}_{\mathbf{u_i}}+\mathbf{G}_{m1,n1}} \alpha_{\mathbf{k}_{\mathbf{u_i}}+\mathbf{G}_{m2,n2}} E^1_{m1,n1} E^1_{m2,n2} \exp[-i\mathbf{G}_{m1-m2,n1-n2} \cdot \mathbf{r} + i(\phi_{m1,n1,\mathbf{u_i}} - \phi_{m2,n2,\mathbf{u_i}})] \\ & + \sum_{m1,n1,cd\mathbf{u_i}} \sum_{m2,n2,cd\mathbf{u_i}} \alpha_{\mathbf{k}_{\mathbf{u_i}}+\mathbf{G}_{m1,n1}} \alpha_{\mathbf{k}_{\mathbf{u_i}}+\mathbf{G}_{m2,n2}} E^0_{m1,n1} E^1_{m2,n2} \exp(2i\mathbf{k}_{\mathbf{u_i}} \cdot \mathbf{r} + i\mathbf{G}_{m1+m2,n1+n2} \cdot \mathbf{r} - i\phi_{m2,n2,\mathbf{u_i}}) \\ & + \sum_{m1,n1,cd\mathbf{u_i}} \sum_{m2,n2,cd\mathbf{u_i}} \alpha_{\mathbf{k}_{\mathbf{u_i}}+\mathbf{G}_{m1,n1}} \alpha_{\mathbf{k}_{\mathbf{u_i}}+\mathbf{G}_{m2,n2}} E^1_{m1,n1} E^0_{m2,n2} \exp(-2i\mathbf{k}_{\mathbf{u_i}} \cdot \mathbf{r} - i\mathbf{G}_{m1+m2,n1+n2} \cdot \mathbf{r} + i\varphi_{m1,n1,\mathbf{u_i}}). \end{aligned} \quad (5)$$

This simplifies in

$$\begin{aligned} I_{\text{int},\mathbf{u_i}}(\mathbf{r},\lambda) = & \sum_{m,n,cd\mathbf{u_i}} (\alpha_{\mathbf{k}_{\mathbf{u_i}}+\mathbf{G}_{m,n}})^2 [E^{0\,2}_{m,n} + E^{1\,2}_{m,n} + 2E^0_{m,n} E^1_{m,n} \cos(2\mathbf{k}_{\mathbf{u_i}} \cdot \mathbf{r} + 2\mathbf{G}_{m,n} \cdot \mathbf{r} - \phi_{m,n,\mathbf{u_i}})] \\ & + 2 \sum_{m1,n1,cd\mathbf{u_i}} \sum_{m2>m1,n2,cd\mathbf{u_i}} \alpha_{\mathbf{k}_{\mathbf{u_i}}+\mathbf{G}_{m1,n1}} \alpha_{\mathbf{k}_{\mathbf{u_i}}+\mathbf{G}_{m2,n2}} [E^0_{m1,n1} E^0_{m2,n2} \cos(\mathbf{G}_{m2-m1,n2-n1} \cdot \mathbf{r}) \\ & + E^1_{m1,n1} E^1_{m2,n2} \cos(\mathbf{G}_{m2-m1,n2-n1} \cdot \mathbf{r} + \phi_{m2,n2,\mathbf{u_i}} - \phi_{m1,n1,\mathbf{u_i}}) + E^0_{m1,n1} E^1_{m2,n2} \cos(2\mathbf{k}_{\mathbf{u_i}} \cdot \mathbf{r} + \mathbf{G}_{m2+m1,n2+n1} \cdot \mathbf{r} - \phi_{m2,n2,\mathbf{u_i}}) \\ & + E^1_{m1,n1} E^0_{m2,n2} \cos(2\mathbf{k}_{\mathbf{u_i}} \cdot \mathbf{r} + \mathbf{G}_{m2+m1,n2+n1} \cdot \mathbf{r} + \varphi_{m1,n1,\mathbf{u_i}})]. \end{aligned} \quad (6)$$

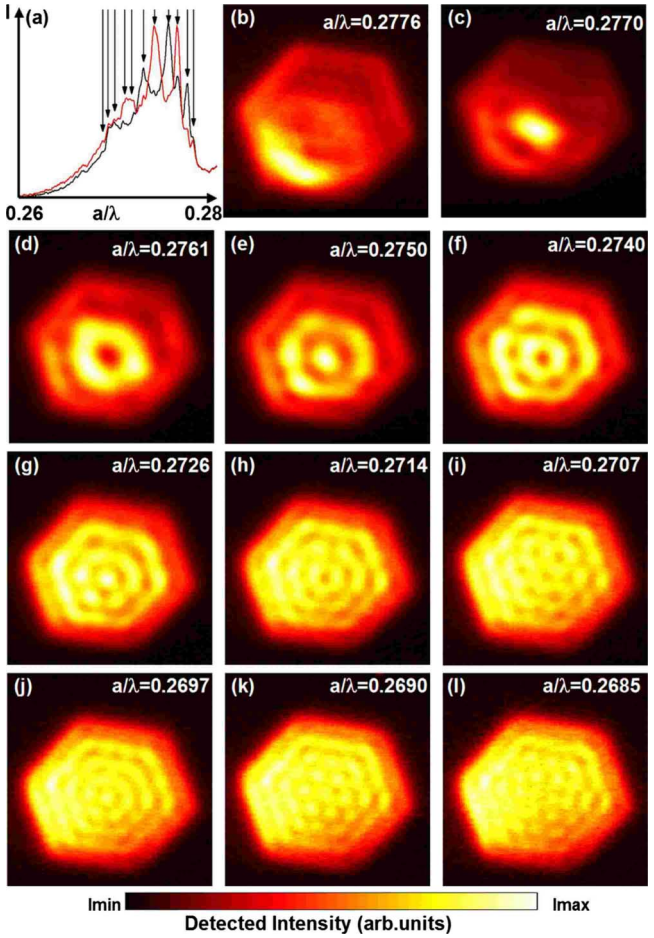

FIG. 4. (Color online) (a). Near-field spectra recorded for the optimal probe position in order to optimize the visibility between the different PL peaks of the 2DPC second band. (b)–(l) Near-field images corresponding to the different PL peaks. The scan size is $25 \times 25\ \mu m^2$.

In Eq. (6) the first term represents the interferences of the Bloch waves *inside the* 2DPC while the other terms represent the interferences of orthogonal Bloch wave harmonics inside the *near-field probe*. In addition, since the near-field probe has a collection efficiency which drastically decreases as the projection of the wave vector along the probe axis decreases,[19] the terms with $m_1=m_2=0$, which implies $n_1=n_2=0$, are expected to be predominant on the near-field measurements. Thus, in a first approach, the light intensity detected by the near-field probe can be reduce to Eq. (7), similar to that one of classical two-wave interferences,

$$I_{\text{int},\mathbf{u_i}}(\mathbf{r},\lambda) = \alpha^2_{\mathbf{k_{u_i}}}(E^{0}_{0,0}{}^2 + E^{1}_{0,0}{}^2)\left[1 + 2\frac{E^0_{0,0}E^1_{0,0}}{E^{0}_{0,0}{}^2 + E^{1}_{0,0}{}^2}\cos(2i\mathbf{k_{u_i}} - i\varphi_{0,0,\mathbf{u_i}})\right]. \quad (7)$$

Consequently, on the near-field spectra presented previously, the spectral location of the cavity resonances is entirely defined by the cavity size; their relative contrast only depends on the probe position. We reported in Fig. 4(a) [respectively, Fig. 5(a)] two PL spectra, corresponding to the second band (respectively, the third band) of the 2DPC, recorded for the two probe positions leading to a maximal contrast between the peaks. On the figure, the PL peaks appear alternatively on the two PL spectra, each PL peak corresponding to a single resonance of the Bloch wave cavity.

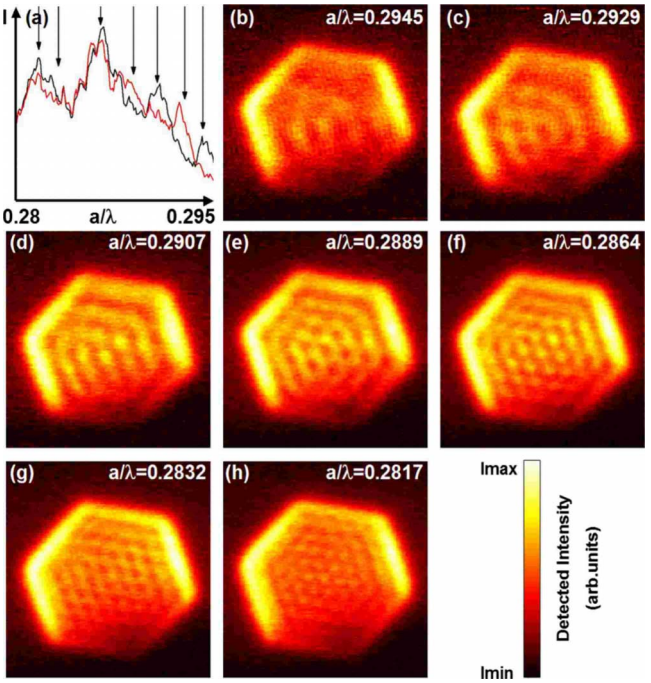

FIG. 5. (Color online) (a). Near-field spectra recorded for the optimal probe position in order to optimize the visibility between the different PL peaks of the 2DPC third band. (b–h) Near-field images corresponding the different PL peaks. The scan size is $25 \times 25\ \mu m^2$.

V. OPTICAL NEAR-FIELD MAPPING IN DIRECT SPACE AND IN FOURIER SPACE

By scanning the SNOM probe above the structure, we recorded $25 \times 25\ \mu m^2$ near-field maps associated to each PL peak. This image size is chosen to visualize the whole structure in the direct space as well as the terms of Eq. (7) associated to the interferences between the firsts Brillouin zones in the Fourier space. The experimental images corresponding to the successive PL peaks of the 2DPC second band (respectively, the third band) are reported in Fig. 4 (respectively, Fig. 5). A rapid glance at all the near-field maps shows that they all exhibit the *C*6 symmetry of the structure. Moreover, one can observe that as the PL-peak-reduced frequency decreases, the number of nodes and antinodes increases one by one on the corresponding near-field map. This obviously implies that the periodicity of the field distribution decreases at the same time. Such a phenomenon is clearly visible for the second band of the 2DPC as well as for the third band.

In addition, this evolution is confirmed by the Fourier space images plotted in Fig. 6 (respectively, Fig. 7) associated to the near-field images in Fig. 4 (respectively, Fig. 5) for the second (respectively, third) band. On these Fourier

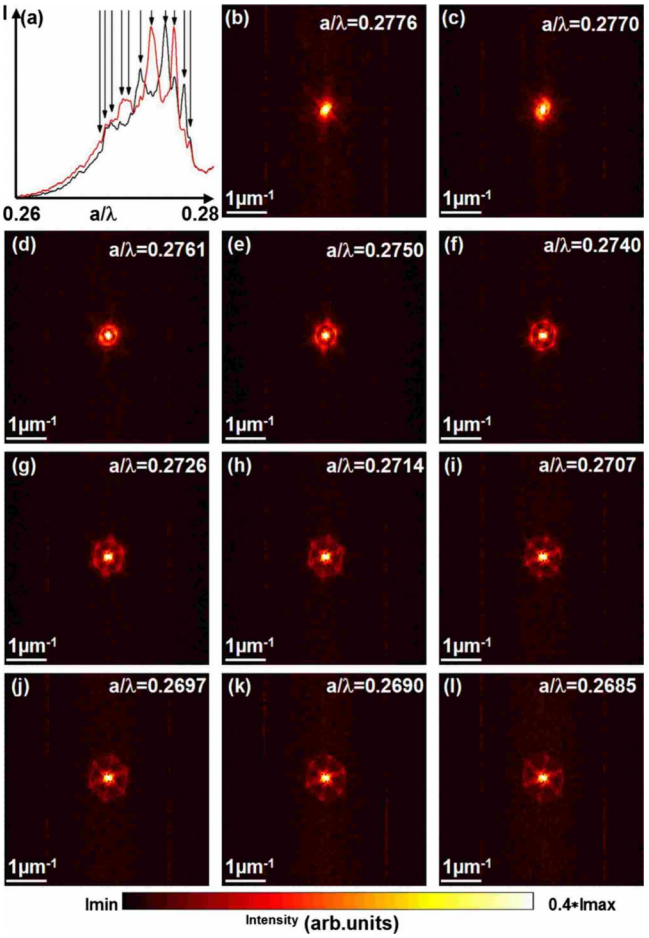

FIG. 6. (Color online) (a) Same near-field spectra as in Fig. 4(a). (b)–(l) Fourier space images associated to the near-field images presented in Figs. 4(b)–4(l).

space maps, one clearly observe that the hexagonal halo is growing up as the reduced frequency decreases, which is related to a decrease of the periodicity in the direct space.

Assuming that this evolution is related to the Bloch wave vector increase associated to a reduced frequency decrease (i.e., that the curvature of the bands is negative), one may be able to recover the band diagram of the 2DPC. According to Eq. (7), for a given wavelength, the measured periodicity $T^{\lambda}_{\mathbf{u_i}}$ of the experimental field distribution maps along the direction $\mathbf{u_i}$ is directly $T^{\lambda}_{\mathbf{u_i}}=\frac{\pi}{k_{\mathbf{u_i}}}$. Thus, by measuring the $T^{\lambda}_{\mathbf{u_i}}$ for each near-field map, which exhibits a clear periodicity, and along the different directions $\mathbf{u_i}$ (three corresponding to ΓM and the three others to ΓK), we determined the wave-vector amplitude, $k_{\mathbf{u_i}}$, of the Bloch waves. The obtained values are superimposed on the theoretical band diagram presented in Fig. 2(a). The error bar of the measurement shown in the figure corresponds to the wave-vector dispersion obtained along the different directions of the structure. The obtained values quantitatively agree with the computed ones, demonstrating the validity of our interpretation. Moreover, according to the curvature of the measured bands, this confirms that the refractive index of the 2DPC is negative.

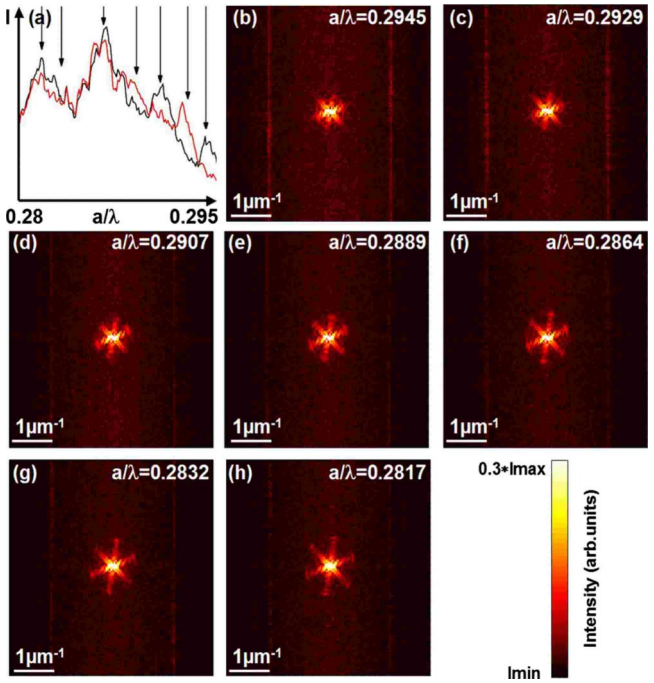

FIG. 7. (Color online) (a) Same near-field spectra as in Fig. 5(a). (b)–(h) Fourier space images associated to the near-filed images presented in Figs. 5(b)–5(h).

VI. DISCUSSION

Finally, we underline that Eq. (7) is only valid if the SNOM probe only collects the wave vectors lying in the first Brillouin zone. This can be visible experimentally by analyzing systematically all the near-field images in the Fourier space. For example, we present in Fig. 8 a comparison between two series of two near-field images obtained at $a/\lambda=0.2726$ with two different probes. The first probe, which is the probe used to obtain Figs. 4 and 5, leads to a single periodicity on the near-field image [Fig. 8(a)]. The second probe that consist in a tapered fiber optical (Lovalite®) leads to two different periodicities: the first one is comparable to that obtained with the first probe and the second one is shorter and is visible on the 6×3 μm^2-zoom insert in Fig. 8(b).

The first periodicity obtained with the two probes is related to the interferences between the Bloch harmonics lying in the first Brillouin zone, i.e., with $m_1=m_2=0$ and visible as a hexagonal halo on the two Fourier space maps in Figs. 8(c) and 8(d).

The second periodicity visible as bright spots highlighted by circles labeled from I to IV in the Fourier space image of Fig. 8(d) resulted from the interferences between the Bloch harmonics lying in the first and in the second Brillouin zones. In light of the measured periodicity (in Fourier space as well as in direct space) and their orientation, we identify the Bloch harmonics that are involved for each point:

(i) The interferences related to the $E^0_{0,0}$ and $E^0_{1,0}$ harmonics (respectively, the $E^0_{0,0}$ and $E^0_{-1,0}$) along the M_1-M_4 direction leads to point I (respectively, point III) on the Fourier space map.

(ii) The interferences related to the $E^0_{0,0}$ and $E^0_{0,1}$ harmonics (respectively, the $E^0_{0,0}$ and $E^0_{0,-1}$) along the M_2-M_5 di-

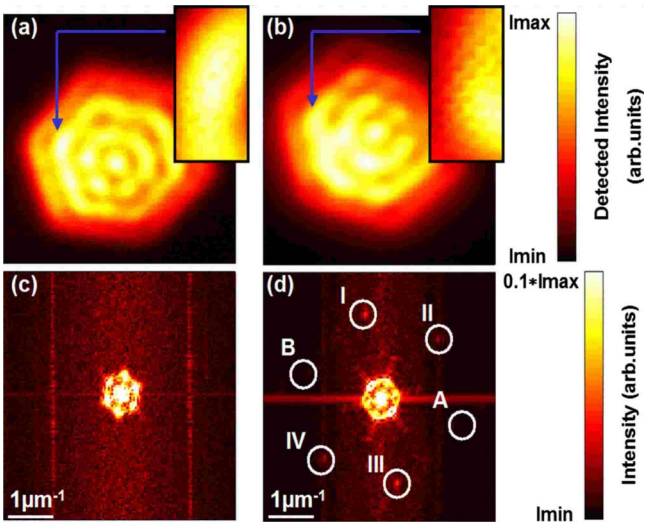

FIG. 8. (Color online) [(a) and (b)] Near-field images obtained at $a/\lambda=0.2726$ with two different probes. The scan size is 25×25 μm^2. The insert shows a 3×6 μm^2 zoom on the near-field image. [(c) and (d)] Fourier space images associated with the near-field images presented in (a) and (b). The circles labeled from I to IV highlight the bright spots inside them and correspond to the interference between a Bloch harmonic lying in the first Brillouin zone and a Bloch harmonic lying in the second Brillouin zone. The A and B circles point two expected positions of bright spots that are not observed experimentally.

rection leads to point II (respectively, point IV).

Let us emphasize that one could expect bright spots inside circles A and B on the Fourier space map with respect to the *C*6 symmetry of the whole structure. The expected spot A would correspond to the interferences between the $E^0_{0,0}$ and $E^0_{-1,1}$ Bloch harmonics, while the expected spot B would correspond to interferences between the $E^0_{0,0}$ and $E^0_{1,-1}$ Bloch harmonics. As said previously and as reported elsewhere,[19] since the near-field probe has a collection efficiency which drastically decreases as the projection of the wave vector along the probe axis decreases, the collection efficiency of the $E^0_{1,-1}$ Bloch harmonic would be the same as the collection efficiency of the $E^0_{0,1}$ Bloch harmonic since they exhibit the same wave-vector projection along the probe axis. Consequently, the nonobservation of the bright spots at A and B on the Fourier space map implies that our near-field probe collection efficiency is not perfectly isotropic which leads to a drop of collection efficiency from the $E^0_{0,1}$ to the $E^0_{-1,1}$ Bloch harmonics (as well as from the $E^0_{1,0}$ to the $E^0_{1,-1}$ Bloch harmonics).

In the case of all the presented near-field images in direct space in Figs. 4 and 5, one can clearly observe on the corresponding Fourier space map of Figs. 6 and 7 that it is only the interferences related to the $E^0_{0,0}$ Bloch harmonics that are measured whatever the relative amplitudes[20] of the (m^{st},n^{st})-Bloch harmonics. This is in good agreement with the limits of Eq. (7), which we have discussed in this section.

At last, in light of the band diagram of the 2DPC in Fig. 2, we notice that one could also expect to evidence experimentally, on the near-field images as well as on the near-field spectra, the existence of an overlap between the second and the third bands for reduced frequency ranging from 0.2685 to 0.2776. However, with respect to the previous discussion, inside the first Brillouin zone, the projection of the second band wave vector along the near-field probe axis is much larger than that of the third band. Consequently, as long as the used near-field probe only collects Bloch harmonics lying inside the first Brillouin zone, the second band collection efficiency remains larger than the third band one.

VII. CONCLUSION

Finally, in light of these previous considerations and results, we will now underline the influence of the negative refractive index on the field distribution within the 2DPC structure. As demonstrated earlier, since the whole structure supports several standing Bloch waves depending on discrete wavelengths, one can consider this structure as a Fabry-Perot-type cavity in which the Bloch waves are bouncing in a negative index media. In a classical right-handed cavity (RHC), i.e., with a positive refractive index, it is well known that the number of nodes and antinodes of the standing wave supported by the cavity increases as the wavelength of the cavity resonances decreases. In the case of a left-handed cavity (LHC) such a phenomenon is reversed and the number of nodes and antinodes of the standing wave supported by the cavity increases as the wavelength increases. This clearly corresponds to the operating regime we observed experimentally on the near-field maps in Figs. 4 and 5. Consequently, one can consider that the reported 2DPC structure acts as a left-handed cavity.

In conclusion, we reported the direct visualization, using a scanning near-field optical microscope, of the spatial and spectral properties of 2D Bloch waves in a negative index photonic crystal. We have shown that the light distribution within the structure is driven by the interferences of the two-dimensional Bloch wave. Our analysis is supported by a direct comparison between the dispersion curves recovered in light of the experimental observations and the theoretical band diagram of the photonic crystal. At last, we evidenced that the whole two-dimensional photonic crystal structure studied in this work acts as a left-handed cavity. This work illustrates the unique properties of negative refractive index media to reverse the well-known physical effects relying on electromagnetic waves propagation and may open a route of investigation toward left-handed media applications.[2]

ACKNOWLEDGMENTS

The heterostructure was grown by Philippe Regreny at INL. Wafer bonding was performed in collaboration with CEA-LETI. This work was partly funded by the French Ministry for Research, through the ACI "CHABIP" project and by the European Network of Excellence ePIXnet through Grant No. IST-004525.

*Corresponding author: benoit.cluzel@u-bourgogne.fr

[1] V. G. Veselago, Sov. Phys. Usp. **10**, 509 (1968).
[2] U. Leonhardt and T. G. Philbin, New J. Phys. **9**, 254 (2007).
[3] J. B. Pendry, Phys. Rev. Lett. **85**, 3966 (2000).
[4] R. A. Shelby, D. R. Smith, and S. Schultz, Science **292**, 77 (2001).
[5] M. Notomi, Phys. Rev. B **62**, 10696 (2000).
[6] C. Luo, S. G. Johnson, J. D. Joannopoulos, and J. B. Pendry, Phys. Rev. B **68**, 045115 (2003).
[7] T. Decoopman, G. Tayeb, S. Enoch, D. Maystre, and B. Gralak, Phys. Rev. Lett. **97**, 073905 (2006).
[8] A. Berrier, M. Mulot, M. Swillo, M. Qiu, L. Thylen, A. Talneau, and S. Anand, Phys. Rev. Lett. **93**, 073902 (2004).
[9] E. Schonbrun, T. Yamashita, W. Park, and C. J. Summers, Phys. Rev. B **73**, 195117 (2006).
[10] R. Gajic, R. Meisels, F. Kuchar, and K. Hingerl, Phys. Rev. B **73**, 165310 (2006).
[11] C. Monat, C. Seassal, X. Letarte, P. Regreny, P. Rojo-Romeo, P. Viktorovitch, M. Le Vassor d'Yerville, D. Cassagne, J. P. Albert, E. Jalaguier, S. Pocas, and B. Aspar, Appl. Phys. Lett. **81**, 5102 (2002).
[12] B. Cluzel, V. Calvo, T. Charvolin, E. Picard, P. Noé, and E. Hadji, Appl. Phys. Lett. **89**, 201111 (2006).
[13] P. Kramper, M. Kafesaki, C. M. Soukoulis, A. Birner, F. Müller, U. Gösele, R. B. Wehrspohn, J. Mlynek, and V. Sandoghdar, Opt. Lett. **29**, 174 (2004).
[14] B. Cluzel, D. Gérard, E. Picard, T. Charvolin, F. de Fornel, and E. Hadji, J. Appl. Phys. **98**, 86109 (2005).
[15] H. Gersen, T. J. Karle, R. J. P. Engelen, W. Bogaerts, J. P. Korterik, N. F. van Hulst, T. F. Krauss, and L. Kuipers, Phys. Rev. Lett. **94**, 123901 (2005).
[16] N. Louvion, D. Gérard, J. Mouette, F. de Fornel, C. Seassal, X. Letartre, A. Rahmani, and S. Callard, Phys. Rev. Lett. **94**, 113907 (2005).
[17] H. Gersen, T. J. Karle, R. J. P. Engelen, W. Bogaerts, J. P. Korterik, N. F. van Hulst, T. F. Krauss, and L. Kuipers, Phys. Rev. Lett. **94**, 073903 (2005).
[18] M. Lebental, N. Djellali, C. Arnaud, J. S. Lauret, J. Zyss, R. Dubertrand, C. Schmit, and E. Bogomolny, Phys. Rev. A **76**, 023830 (2007).
[19] S. I. Bozhevolnyi, V. S. Volkov, T. Sondergaard, A. Boltasseva, P. I. Borel, and M. Kristensen, Phys. Rev. B **66**, 235204 (2002).
[20] B. Lombardet, L. A. Dunbar, R. Ferrini, and R. Houdré, J. Opt. Soc. Am. B **22**, 1179 (2005).